Structure

Crystal Structure of Atg13 LIR/LC3 Complex
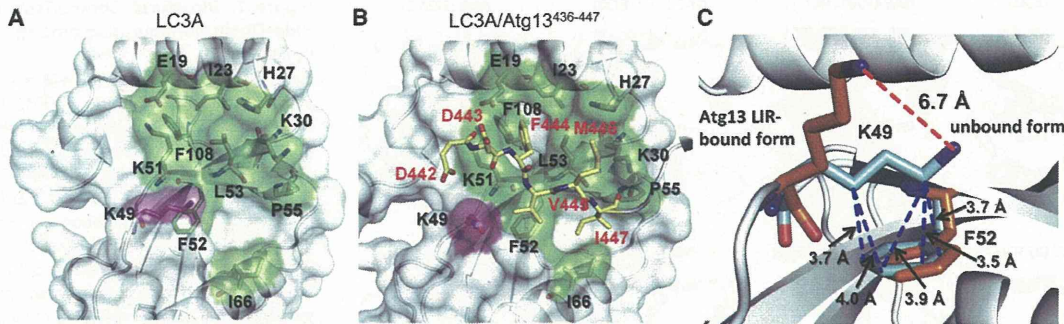

Figure 5. Structural Comparison between the Uncomplexed and the Atg13 LIR Complexed Forms of LC3A

(A and B) LC3A and LC3A/Atg13[436–447] are shown in ribbon and transparent surface representation. LIR and its interaction residues are shown in stick representation. Carbon atoms of LIR, Lys49, and other residues are colored yellow, magenta, and green, respectively. Oxygen and nitrogen atoms are in red and blue, respectively.

(C) Close-up view of Lys49 and Phe52. Carbon atoms of the uncomplexed form and Atg13 LIR complexed form of LC3A are colored in orange and cyan, respectively.

mouse embryonic fibroblast cells stably expressing GFP-tagged LC3A[WT], LC3A[K49A], or LC3A[K51A] and tested for LC3A positive puncta formation (Figures 8A and 8B). Western blotting showed similar GFP-LC3A expression levels in each stable cell line (Figure S7). LC3A[WT] formed puncta in the cells with nutrient-rich conditions (39 ± 12 dots/cell), and the number of puncta was significantly increased under starvation conditions (134 ± 18 dots/cell). The number of puncta further increased (188 ± 29 dots/cell) after treatment with Baf A1, an inhibitor of lysosomal acidification. Taken together, these data indicate that GFP-LC3A[WT]-positive autophagosomes are under active autophagy flux.

Surprisingly, cell lines expressing GFP-tagged LC3A[K49A] and LC3A[K51A] did not form any puncta in nutrient-rich conditions (2 ± 1 dots/cell in K49A; 12 ± 7 dots/cell in K51A) and formed even fewer puncta in starvation conditions (88 ± 36 dots/cell in K49A; 100 ± 15 dots/cell in K51A), despite the observation above that LC3A[K49A] has significantly increased binding to the Atg13 LIR, whereas LC3A[K51A] has reduced the binding abilities (Figure 6D). Moreover, LC3-positive puncta for LC3A[K49A] and LC3A[K51A] were also fewer than those of LC3A[WT] in the presence of Baf A1, indicating that autophagy flux was decreased. These data also suggest that the reduced number of puncta formation results from the defect in autophagosome formation, but not enhancement of autophagosome degradation. Overall, these data suggest that there is a specific range, at least from 10 μM (LC3C) to 60 μM (LC3B), with respect to Atg13 LIR binding affinity for LC3A. If either too high or too low, autophagosome formation is decreased.
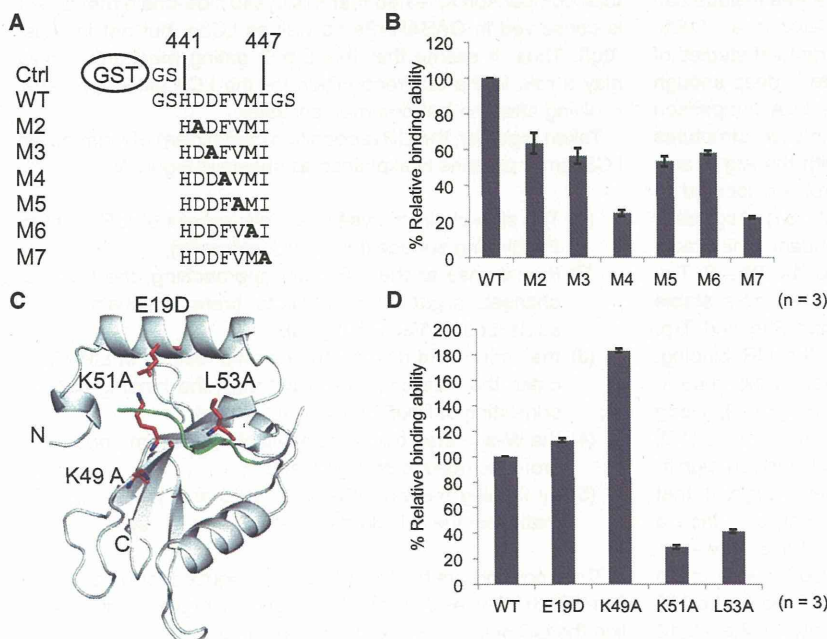

Figure 6. Mutational Analyses of the Interactions between Atg13 and LC3

(A) Schematic representation of mutants for Ala scanning.

(B and D) Relative binding abilities of point mutants of Atg13 or LC3A compared with WT were measured by an SPR biosensor and expressed in percentages. Each value represents the mean ± SD. The sensorgrams are shown in Figure S4.

(C) Ribbon diagram of the Atg13 LIR-fused LC3A structure highlighting the substituted residues (red stick representation) and the LIR (ribbon representation and colored line).
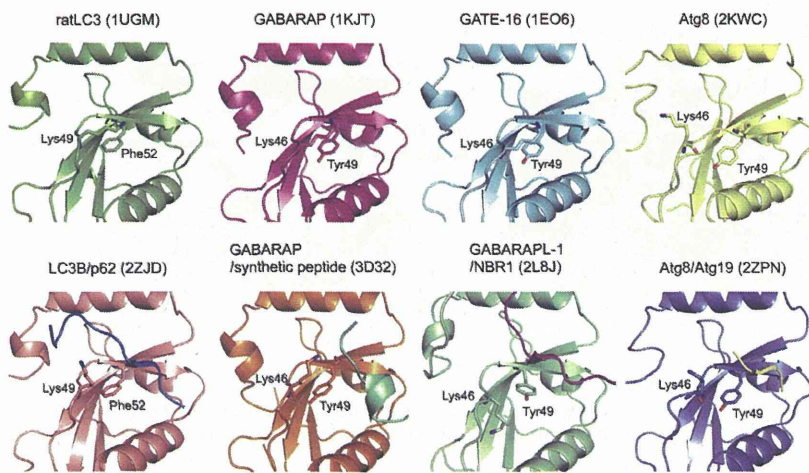
Figure 7. Structural Comparison of Lys49 Side-Chain Configuration among LC3 Family Proteins

Corresponding residues to Lys49 and Phe52 of LC3A in ratLC3 (PDB code 1UGM), GABARAP (1JKT), GATE-16 (1EO6), and Atg8 (2KWC) as uncomplexed form, and LC3B/p62 (2ZJD), GABARAP/synthetic peptide (3D32), GABARAP-L1/NBR1 (2L8J), and Atg8/Atg19 (2ZPN) as LIR-bound form are shown in ribbon representation in green, magenta, cyan, magenta, yellow, salmon, orange, lime green, and slate, and the peptides are colored marine blue, lime green, purple, and yellow orange, respectively. Side-chain atoms are colored red for oxygen and blue for nitrogen.

DISCUSSION

Recently Alemu et al. (2012) reported that Atg8 family proteins interact with ULK1/2, FIP200, and Atg13 and that this interaction is mediated by a LIR motif, which together suggested that Atg8 proteins play a role in scaffolding for the Atg1/ULK1 complex assembly. However, the molecular mechanism underpinning the interaction between the LIR and Atg8 family proteins was unclear. In this study, we have determined the crystal structures of the three LC3 isoforms in complex with the Atg13 LIR to delineate the key interactions between the two proteins, and we verified them by mutational analysis and in vivo studies.

We have identified that the LC3 binding site of Atg13 spans residues 441–447 (HDDFVMI) and provides the structural basis for the binding. Although the LIR motif was originally defined as xxxW/YxxL/I/V, it was recently reported that a Phe residue can also be tolerated at the aromatic position (Satoo et al., 2009; Kraft et al., 2012; Alemu et al., 2012). Our structural studies of the LC3 isoforms demonstrate that the W-site is deep enough to bury the bulky aromatic side-chains (Figure 5). A comparison of the Atg13 LIR and p62 LIR in those complexed structures shows that the LC3 residues that interact with the Atg13 aromatic residue (Atg13 LIR, Phe; p62 LIR, Trp) are located at the bottom of the hydrophobic pocket (Table S1). According to Alemu et al. (2012), Trp is the most abundant amino acid at the aromatic position in the LIR motifs (Trp, 14; Phe, 8; Tyr, 4; in 26 LIR motifs), suggesting that Trp forms more stable hydrophobic interactions with the W-site than Phe and Trp. However the W-site is not formed without the LIR binding, in contrast with the L-site, which is open even in the uncomplexed form. Our SPR biosensor analysis (Figure 6), along with previous reports (Noda et al., 2008; Alemu et al., 2012), demonstrates that mutation of the Leu/Ile/Val position significantly reduces binding. Taken together, these suggest that the L-site recognizes Leu/Ile/Val in the LIR first, and then a structural rearrangement occurs to open the W-site. However, binding to the L-site is not sufficient to stabilize the interaction alone, given that mutation of the aromatic residue in the LIR also significantly decreases the binding affinity of the Atg13

peptide to LC3. Accordingly, the W-site probably locks the interaction by burying the bulky part of an aromatic residue.

Our structural analysis demonstrates that Lys49 undergoes a significant structural rearrangement upon the LIR binding (Figure 5). In the uncomplexed structures, the side-chain of Lys49 makes hydrophobic interactions with the aromatic ring of Phe52, closing over the W-site and preventing binding. However, in our complexed structures, Val445 in the Atg13 LIR exists on the surface of Phe52, and Lys49 rearranges its conformation to interact with Val445, which is not observed in the complex structure with p62 LIR. Moreover, our SPR biosensor experiments demonstrate that the LC3A^{K49A} mutant, which we predicted would be in an open conformation, increased the relative binding ability to Atg13 LIR (Figure 6D). These data suggested that the interaction between Lys49 and Val445 does not stabilize this complex, but that the side-chain conformational change of Lys49 is important for recognition of the LIR, probably to open the surface covered by Lys49 and expose the W-site. The structural comparison revealed that this Lys49 side-chain movement is conserved in GABARAPs as well as LC3s, but not in yeast Atg8. Thus, it seems that this Lys49 gating mechanism may play a role in the LIR recognition for the LC3 family proteins, evolving after the last common ancestor.

Taken together, the LIR recognition mechanism of mammalian LC3 family proteins is explained as shown in Figure 9.

(1) The side-chain of Lys49 restricts access of LIR motif to the binding surface (Figure 9C, magenta),
(2) in response to the LIR motif approaching, the L-site is changed slightly and accepts branched-chain amino acids (Leu/Ile/Val; Figure 9B),
(3) the amino acid next to an aromatic residue in LIR dislocates the side-chain of Lys49 from the binding surface consisting of Phe52 (Figure 9C, green),
(4) the W-site then becomes available to accommodate the aromatic residue of Atg13, and
(5) by flipping the side-chains of Ile23 and Leu53, an aromatic residue is locked (Figure 9D).

Thus, not only are the W- and L-sites required for binding, but Lys49 is the key residue for LIR recognition, in particular controlling the LIR access to the interaction surface.
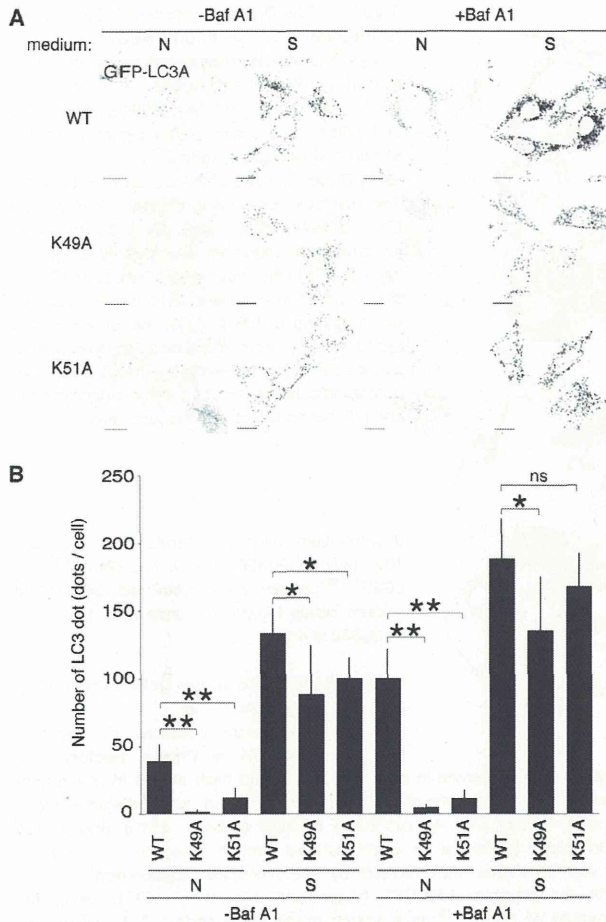
A

B

Figure 8. The Effect of LC3 Mutations on Autophagosome Formation and Autophagy Flux

(A) MEFs stably expressing the indicated constructs were cultured in nutrient-rich medium (N) or EBSS (S) with or without bafilomycin A1 (Baf A1) for 1 hr. Bars indicate 20 μm.

(B) The numbers of LC3 puncta in cells were counted in >30 cells. Each value represents the mean ± SD. Statistical analysis was performed by Student's t test: *p < 0.05, **p < 0.01; ns, not significant.

To establish the biological importance of Lys49, we assessed the effect of substituting LC3A Lys49 or Lys51 with Ala on autophagosome formation using fluorescence microscopy. Because the binding of LC3A^{K49A} to the Atg13 LIR increased markedly as compared with LC3A^{WT}, we expected that this mutation would increase the number of autophagosomes under starvation conditions by enhancing the interaction with LIR. Surprisingly, however, both the K49A and K51A mutants showed a significant decrease in autophagosome formation, especially under nutrient-rich conditions, in which selective autophagy is predominant over macroautophagy induced by stimulus. On the other hand, under starvation conditions, where the Atg1/ULK1 complex is activated by TORC1 and initiates macroautophagy, the K49A mutation demonstrated a greater decrease in autophagosome formation than did K51A mutation, with or without Baf A1. Although this experiment cannot distinguish between specific

binding partners, it demonstrates the importance of the Lys49 side-chain configuration in vivo and suggests that only a specific affinity between LC3 and its binding partners is required for recruiting substrates to the isolation membrane and proper autophagosome formation.

In conclusion, we proposed a LIR recognition mechanism for the mammalian LC3 family proteins, whereby LIR binding is regulated by Lys49 side-chain gating, and demonstrate that specific binding affinities (the expected range is from 10 μM to 60 μM) by this mechanism are required for recruiting its binding partners to autophagosome in both starvation-induced and selective autophagy.

EXPERIMENTAL PROCEDURES

Expression Plasmids

For the mammalian expression vectors, ULK1 complex subunits (Atg101, Atg13, ULK1, and FIP200), and LC3s, cDNA open reading frames (ORFs) were subcloned into KpnI/XhoI sites of pCAG-OSF or pCAG-Myc vectors, as described previously (Madaule et al., 1998; Bajorek et al., 2009). For yeast two-hybrid vectors, cDNA ORFs were subcloned into EcoRI/BamHI sites (Atg13, Atg101, LC3A, and LC3C) or NcoI/BamHI sites (GABARAP) of pGADT7 or pGBKT7. For retroviral expression vectors, LC3A cDNA ORFs were subcloned into EcoRV sites of pMRX retroviral vector. For bacterial expression vectors, Atg13 truncation mutants, LC3A$^{2-121}$, LC3B$^{2-119}$, and LC3C$^{8-125}$ were generated by PCR and inserted into pGEX-4T-1 (Atg13, BamHI/EcoRI site; LC3A, EcoRI/SalI site; LC3C, BamHI/EcoRI site; GE Healthcare), pCold TF (Atg13, BamHI/EcoRI site; Clontech), the BamHI/EcoRI site of pET30 (Invitrogen) deleted S-tag, and Enterokinase site (designated pET30ΔSE) by QuickChange mutagenesis kit (Stratagene) using the oligonucleotide pair 5′-CTGGTGCCACGCGGATCCGAATTCGAGCTC-3′ and 5′-GAGCTCGAATT CGGATCCGCGTGGCACCAG-3′. For construction of the GST-fused peptide, the oligonucleotide pair (5′-GATCCTGAGATATCGACTCGAGG-3′ and 5′-AATTCCTCGAGTCGATATCTCAG-3′) was inserted into the BamHI/EcoRI site of pGEX-4T-1, designated pGEX-4T_BS (BamHI-Stop). The chimera proteins of Atg13 LIR-fused LC3 isoforms and GST-fused Atg13 LIR peptides were constructed by inserting a pair of double-stranded oligonucleotides into the BamHI sites of pET30ΔSE/LC3 isoforms and pGEX-4T_BS, respectively. Point mutants of LC3A were generated using the QuickChange mutagenesis kit.

Cell Cultures

HEK293T and mouse embryonic fibroblast (MEF) cells were maintained in Dulbecco's modified Eagle's medium supplemented with 10% fetal calf serum. Stable transformants were selected in growth medium with 1 μg/ml puromycin. For immunofluorescence experiments, MEF cells were seeded onto coverslips and cotransfected at 50%–60% confluence.

Coprecipitation and Western Blotting Assays

HEK293T cells were seeded (3 × 10^6 cells/55 cm^2 dish) and cotransfected with each relevant expression plasmid (polyethylenimine 25,000 kDa; Polysciences), as described (Durocher et al., 2002). Cells were harvested 48 hr posttransfection by incubation in lysis buffer (50 mM Tris-HCl, pH 7.4, 150 mM NaCl) supplemented with protease inhibitor cocktail (Sigma) and 1% Triton X-100. Lysates were clarified by centrifugation (18,000 × g, 10 min, 4°C) and incubated with Strep-Tactin Sepharose for 2 hr (IBA). The resin was washed four times with wash buffer (20 mM Tris-HCl, pH 7.4, 150 mM NaCl) supplemented with 0.1% Triton X-100, and bound proteins were detected by mass spectrometry or western blotting.

Yeast Two-Hybrid Binding Assays

Directed yeast two-hybrid assays were performed using the Matchmaker GAL4 Yeast Two Hybrid 3 System (Clontech). Briefly, Saccharomyces cerevisiae AH-109 was cotransformed with pGADT7 or pGBKT7 cloning vector (Clontech) containing the inserts of interest. The transformed yeast colonies were grown for 3 days at 30°C on yeast-extract-peptone-dextrose plates
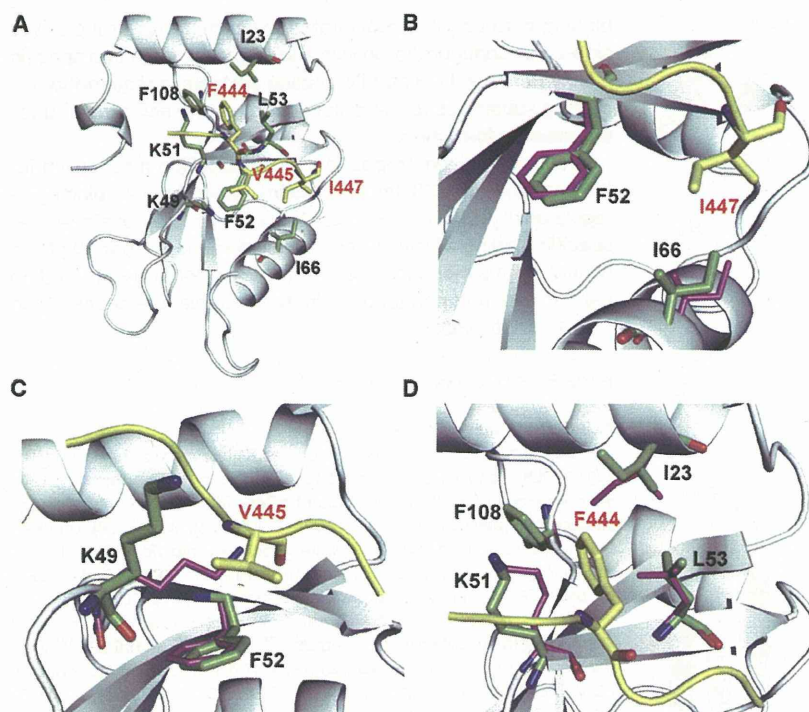
Figure 9. The Binding between LC3 and LIR Is Regulated by Structural Rearrangement of Lys49 Side-Chain and Hydrophobic Interaction by Phe444 and Ile447

(A) Ribbon diagram of LC3A and LIR colored white and yellow. Side chains of binding residues are shown in stick representation.

(B–D) Close-up views of the critical binding sites. The residues surrounding Phe444 (the W-site) (D) and Ile447 (the L-site) (B) undergo subtle structural rearrangement and form hydrophobic interactions. In the uncomplexed structure (C), the side-chain of Lys49 covers LIR interaction surface. Upon binding of LIR to LC3, the side-chain of Lys49 detached from Phe52 an open hydrophobic surface consisting of Lys49 and Phe52. Green and purple indicate the residues in the uncomplexed and LIR-bound structures, respectively.

with minus Leu, minus Trp selection. From 10 to 100 colonies were pooled, resuspended in a liquid culture of Sabourand dextrose broth (minus Leu, minus Trp), selected on Sabourand dextrose broth (minus Leu, minus Trp, minus Ade, minus His) plates, and allowed to grow for 3 days.

Purification of Recombinant Proteins and GST Pulldown Assay

All proteins were expressed in *E. coli* BL21(DE3) cells at 25°C by 0.3 mM isopropyl β-D-1-thiogalactopyranoside induction for 16 hr. Cells were harvested and lysed in PBS (Wako) or Tris-buffered saline (20 mM Tris-HCl, pH 9.0, 100 mM NaCl) including 1% Triton X-100 and immobilized onto GS4B (GE Healthcare) or Ni-NTA (Invitrogen), respectively. Immobilized proteins were cleaved with thrombin (GE Healthcare) at 22°C or 4°C for 16 hr. Eluted proteins were further purified by gel filtration (Superdex 200 10/300 GL; GE Healthcare). For GST pulldown assays, GST-fused LC3s and Atg13 deletion mutants were attached to GS4B and incubated with purified proteins for 1 hr at 4°C. After washing three times with PBS, the bound proteins were analyzed by SDS-PAGE followed by CBB staining.

Crystallization

Initial crystallization screening was performed using kits from Hampton Research (Crystal Screen and Crystal Screen 2, PEG/Ion Screen 1 and 2, MembFac and Index), from Emerald BioStructures (Wizard I and II, Cryo I and II), and from Molecular Dimensions (Stura Footprint Screens) by sitting-drop vapor diffusion method at 4°C and/or 20°C using an automatic crystallization robot system (Hiraki et al., 2006). The crystals of LC3A$^{2-121}$, LC3C$^{8-125}$, Atg13$^{436-447}$-LC3A$^{2-121}$, Atg13$^{436-447}$-LC3B$^{2-119}$, and Atg13$^{436-447}$-LC3C$^{8-125}$ were obtained using PEG/Ion Screen 2 condition No. 4 (0.2 M sodium malonate, pH 5.0, 20% [w/v] PEG3350) at 20°C, PEG/Ion Screen condition No. 48 (0.2 M di-ammonium hydrogen citrate, pH 5.1, 20% [w/v] PEG3350) at 4°C, MembFac condition No. 1 (0.1 M sodium acetate trihydrate, pH 4.6, 0.1 M sodium chloride, 12% [v/v] 2-methyl-2,4-pentanediol) at 4°C, Index condition No. 94 (0.2 M sodium citrate tribasic dihydrate, 20% [w/v] PEG3350) at 20°C, and Crystal Screen condition No. 37 (0.1 M sodium acetate trihydrate, pH 4.6, 8% [w/v] PEG4000) at 4°C, respectively. For crystallization of LC3C$^{8-125}$ and Atg13$^{436-447}$-LC3B$^{2-119}$, crystallization conditions were optimized manually by the hanging-drop vapor diffusion method. Finally, LC3C$^{8-125}$ proteins were crystallized using 0.5 M

di-ammonium hydrogen citrate, pH 5.0, and 10% (w/v) PEG3350 at 4°C, and Atg13$^{436-447}$-LC3B$^{2-119}$ proteins were crystallized using 0.1 M sodium citrate tribasic dihydrate and 10% (w/v) PEG3350 at 4°C.

Data Collection, Structure Determination, Refinement, and Analyses

Diffraction data were collected at beamline BL-5A and BL-17A at Photon Factory. The crystals were mounted in nylon fiber loops and flash cooled in a nitrogen-gas stream. The diffraction data were indexed and integrated with Mosflm (Leslie and Powell, 2007) or XDS (Kabsch, 2010) and scaled with Scala (Collaborative Computational Project, Number 4, 1994). All crystal structures were solved by the molecular replacement method with the program MOLREP (Vagin and Teplyakov, 1997), using the structure of LC3B$^{2-119}$ as a search model (PDB code 3VTU). All models were refined with the programs CNS (Brünger et al., 1998) and REFMAC5 (Murshudov et al., 1997). Manual adjustments of the structure were performed with COOT (Emsley and Cowtan, 2004). All of the structural figures were generated with PyMOL (DeLano Scientific), and secondary structures were defined and assigned by the DSSP program (Kabsch and Sander, 1983).

SPR Measurement

Real-time binding analyses were performed using an SPR biosensor (Biacore 2000; GE Healthcare) at 25°C. Anti-GST antibodies were covalently coupled to a CM5 sensor chip (GE Healthcare) using a GST Capture Kit (GE Healthcare). For kinetic and interaction analyses, HBS-P (10 mM HEPES-NaOH, pH 7.4, 150 mM NaCl, 0.005% surfactant P20) was used as running buffer at a flow rate of 20 μl/min. GST and GST-Atg13 mutant proteins were diluted to 20 μg/ml in HBS-P and immobilized on a sensor chip for 180 s via anti-GST antibodies (flow cell 1 was immobilized with GST as a reference cell). LC3 proteins were injected using the Kinject program for 180 s. The sensor surface was regenerated by injecting 60 μl of 10 mM glysine-HCl, pH 2.1. The triplicate data were analyzed by the Scatchard plot (RU versus RU/concentration plot) and the K$_D$ were calculated.

Autophagosome Formation Assay

MEFs were cultured in growth medium or Earle's balanced salt solution (Invitrogen) for 1 hr in the presence or absence of 100 nM Baf A1. MEFs expressing protein-fused GFP were directly observed with a confocal fluorescence microscope (FV1000; Olympus). The number of GFP-LC3A dots was determined by G-count (G-Angstrom). GFP-LC3A expression levels were checked by western blotting (Figure S7).

Structure

Crystal Structure of Atg13 LIR/LC3 Complex

ACCESSION NUMBERS

The atomic coordinates and structure factors have been deposited in the Protein Data Bank with accession codes 3WAL, 3WAM, 3WAN, 3WAO, and 3WAP.

SUPPLEMENTAL INFORMATION

Supplemental Information includes seven figures and two tables and can be found with this article online at http://dx.doi.org/10.1016/j.str.2013.09.023.

REFERENCES

Alemu, E.A., Lamark, T., Torgersen, K.M., Birgisdottir, A.B., Larsen, K.B., Jain, A., Olsvik, H., Øvervatn, A., Kirkin, V., and Johansen, T. (2012). ATG8 family proteins act as scaffolds for assembly of the ULK complex: sequence requirements for LC3-interacting region (LIR) motifs. J. Biol. Chem. 287, 39275–39290.

Bajorek, M., Morita, E., Skalicky, J.J., Morham, S.G., Babst, M., and Sundquist, W.I. (2009). Biochemical analyses of human IST1 and its function in cytokinesis. Mol. Biol. Cell 20, 1360–1373.

Bavro, V.N., Sola, M., Bracher, A., Kneussel, M., Betz, H., and Weissenhorn, W. (2002). Crystal structure of the GABA(A)-receptor-associated protein, GABARAP. EMBO Rep. 3, 183–189.

Brünger, A.T., Adams, P.D., Clore, G.M., DeLano, W.L., Gros, P., Grosse-Kunstleve, R.W., Jiang, J.S., Kuszewski, J., Nilges, M., Pannu, N.S., et al. (1998). Crystallography & NMR system: a new software suite for macromolecular structure determination. Acta Crystallogr. D Biol. Crystallogr. 54, 905–921.

Chan, E.Y., Kir, S., and Tooze, S.A. (2007). siRNA screening of the kinome identifies ULK1 as a multidomain modulator of autophagy. J. Biol. Chem. 282, 25464–25474.

Chan, E.Y., Longatti, A., McKnight, N.C., and Tooze, S.A. (2009). Kinase-inactivated ULK proteins inhibit autophagy via their conserved C-terminal domains using an Atg13-independent mechanism. Mol. Cell. Biol. 29, 157–171.

Collaborative Computational Project, Number 4. (1994). The CCP4 suite: programs for protein crystallography. Acta Crystallogr. D Biol. Crystallogr. 50, 760–763.

Dikic, I., Johansen, T., and Kirkin, V. (2010). Selective autophagy in cancer development and therapy. Cancer Res. 70, 3431–3434.

Durocher, Y., Perret, S., and Kamen, A. (2002). High-level and high-throughput recombinant protein production by transient transfection of suspension-growing human 293-EBNA1 cells. Nucleic Acids Res. 30, E9.

Emsley, P., and Cowtan, K. (2004). Coot: model-building tools for molecular graphics. Acta Crystallogr. D Biol. Crystallogr. 60, 2126–2132.

Funakoshi, T., Matsuura, A., Noda, T., and Ohsumi, Y. (1997). Analyses of APG13 gene involved in autophagy in yeast, Saccharomyces cerevisiae. Gene 192, 207–213.

Hara, T., Takamura, A., Kishi, C., Iemura, S., Natsume, T., Guan, J.L., and Mizushima, N. (2008). FIP200, a ULK-interacting protein, is required for autophagosome formation in mammalian cells. J. Cell Biol. 181, 497–510.

He, H., Dang, Y., Dai, F., Guo, Z., Wu, J., She, X., Pei, Y., Chen, Y., Ling, W., Wu, C., et al. (2003). Post-translational modifications of three members of the human MAP1LC3 family and detection of a novel type of modification for MAP1LC3B. J. Biol. Chem. 278, 29278–29287.

Hemelaar, J., Lelyveld, V.S., Kessler, B.M., and Ploegh, H.L. (2003). A single protease, Apg4B, is specific for the autophagy-related ubiquitin-like proteins GATE-16, MAP1-LC3, GABARAP, and Apg8L. J. Biol. Chem. 278, 51841–51850.

Hiraki, M., Kato, R., Nagai, M., Satoh, T., Hirano, S., Ihara, K., Kudo, N., Nagae, M., Kobayashi, M., Inoue, M., et al. (2006). Development of an automated large-scale protein-crystallization and monitoring system for high-throughput protein-structure analyses. Acta Crystallogr. D Biol. Crystallogr. 62, 1058–1065.

Hosokawa, N., Sasaki, T., Iemura, S., Natsume, T., Hara, T., and Mizushima, N. (2009). Atg101, a novel mammalian autophagy protein interacting with Atg13. Autophagy 5, 973–979.

Ichimura, Y., and Komatsu, M. (2010). Selective degradation of p62 by autophagy. Semin. Immunopathol. 32, 431–436.

Ichimura, Y., Kumanomidou, T., Sou, Y.S., Mizushima, T., Ezaki, J., Ueno, T., Kominami, E., Yamane, T., Tanaka, K., and Komatsu, M. (2008). Structural basis for sorting mechanism of p62 in selective autophagy. J. Biol. Chem. 283, 22847–22857.

Johansen, T., and Lamark, T. (2011). Selective autophagy mediated by autophagic adapter proteins. Autophagy 7, 279–296.

Kabeya, Y., Kawamata, T., Suzuki, K., and Ohsumi, Y. (2007). Cis1/Atg31 is required for autophagosome formation in Saccharomyces cerevisiae. Biochem. Biophys. Res. Commun. 356, 405–410.

Kabsch, W. (2010). XDS. Acta Crystallogr. D Biol. Crystallogr. 66, 125–132.

Kabsch, W., and Sander, C. (1983). Dictionary of protein secondary structure: pattern recognition of hydrogen-bonded and geometrical features. Biopolymers 22, 2577–2637.

Kamada, Y., Funakoshi, T., Shintani, T., Nagano, K., Ohsumi, M., and Ohsumi, Y. (2000). Tor-mediated induction of autophagy via an Apg1 protein kinase complex. J. Cell Biol. 150, 1507–1513.

Kawamata, T., Kamada, Y., Suzuki, K., Kuboshima, N., Akimatsu, H., Ota, S., Ohsumi, M., and Ohsumi, Y. (2005). Characterization of a novel autophagy-specific gene, ATG29. Biochem. Biophys. Res. Commun. 338, 1884–1889.

Kraft, C., Kijanska, M., Kalie, E., Siergiejuk, E., Lee, S.S., Semplicio, G., Stoffel, I., Brezovich, A., Verma, M., Hansmann, I., et al. (2012). Binding of the Atg1/ULK1 kinase to the ubiquitin-like protein Atg8 regulates autophagy. EMBO J. 31, 3691–3703.

Kumeta, H., Watanabe, M., Nakatogawa, H., Yamaguchi, M., Ogura, K., Adachi, W., Fujioka, Y., Noda, N.N., Ohsumi, Y., and Inagaki, F. (2010). The NMR structure of the autophagy-related protein Atg8. J. Biomol. NMR 47, 237–241.

Larkin, M.A., Blackshields, G., Brown, N.P., Chenna, R., McGettigan, P.A., McWilliam, H., Valentin, F., Wallace, I.M., Wilm, A., Lopez, R., et al. (2007). Clustal W and Clustal X version 2.0. Bioinformatics 23, 2947–2948.

Leslie, A.G.W., and Powell, H.R. (2007). Processing diffraction data with mosflm. In Evolving Methods for Macromolecular Crystallography, R.J. Read and J.L. Sussman, eds. (Dordrecht: Springer), pp. 41–51.

Levine, B., and Kroemer, G. (2008). Autophagy in the pathogenesis of disease. Cell 132, 27–42.

Li, M., Hou, Y., Wang, J., Chen, X., Shao, Z.M., and Yin, X.M. (2011). Kinetics comparisons of mammalian Atg4 homologues indicate selective preferences toward diverse Atg8 substrates. J. Biol. Chem. 286, 7327–7338.

Madaule, P., Eda, M., Watanabe, N., Fujisawa, K., Matsuoka, T., Bito, H., Ishizaki, T., and Narumiya, S. (1998). Role of citron kinase as a target of the small GTPase Rho in cytokinesis. Nature 394, 491–494.

Mizushima, N., Levine, B., Cuervo, A.M., and Klionsky, D.J. (2008). Autophagy fights disease through cellular self-digestion. Nature 451, 1069–1075.

Murshudov, G.N., Vagin, A.A., and Dodson, E.J. (1997). Refinement of macromolecular structures by the maximum-likelihood method. Acta Crystallogr. D Biol. Crystallogr. 53, 240–255.

Nakatogawa, H., Ichimura, Y., and Ohsumi, Y. (2007). Atg8, a ubiquitin-like protein required for autophagosome formation, mediates membrane tethering and hemifusion. Cell *130*, 165–178.

Noda, N.N., Kumeta, H., Nakatogawa, H., Satoo, K., Adachi, W., Ishii, J., Fujioka, Y., Ohsumi, Y., and Inagaki, F. (2008). Structural basis of target recognition by Atg8/LC3 during selective autophagy. Genes Cells *13*, 1211–1218.

Noda, N.N., Ohsumi, Y., and Inagaki, F. (2010). Atg8-family interacting motif crucial for selective autophagy. FEBS Lett. *584*, 1379–1385.

Paz, Y., Elazar, Z., and Fass, D. (2000). Structure of GATE-16, membrane transport modulator and mammalian ortholog of autophagocytosis factor Aut7p. J. Biol. Chem. *275*, 25445–25450.

Rogov, V.V., Suzuki, H., Fiskin, E., Wild, P., Kniss, A., Rozenknop, A., Kato, R., Kawasaki, M., McEwan, D.G., Löhr, F., et al. (2013). Structural basis for phosphorylation-triggered autophagic clearance of Salmonella. Biochem. J. *454*, 459–466.

Rozenknop, A., Rogov, V.V., Rogova, N.Y., Löhr, F., Güntert, P., Dikic, I., and Dötsch, V. (2011). Characterization of the interaction of GABARAPL-1 with the LIR motif of NBR1. J. Mol. Biol. *410*, 477–487.

Satoo, K., Noda, N.N., Kumeta, H., Fujioka, Y., Mizushima, N., Ohsumi, Y., and Inagaki, F. (2009). The structure of Atg4B-LC3 complex reveals the mechanism of LC3 processing and delipidation during autophagy. EMBO J. *28*, 1341–1350.

Schlumpberger, M., Schaeffeler, E., Straub, M., Bredschneider, M., Wolf, D.H., and Thumm, M. (1997). AUT1, a gene essential for autophagocytosis in the yeast Saccharomyces cerevisiae. J. Bacteriol. *179*, 1068–1076.

Sugawara, K., Suzuki, N.N., Fujioka, Y., Mizushima, N., Ohsumi, Y., and Inagaki, F. (2004). The crystal structure of microtubule-associated protein light chain 3, a mammalian homologue of Saccharomyces cerevisiae Atg8. Genes Cells *9*, 611–618.

Taherbhoy, A.M., Tait, S.W., Kaiser, S.E., Williams, A.H., Deng, A., Nourse, A., Hammel, M., Kurinov, I., Rock, C.O., Green, D.R., and Schulman, B.A. (2011). Atg8 transfer from Atg7 to Atg3: a distinctive E1-E2 architecture and mechanism in the autophagy pathway. Mol. Cell *44*, 451–461.

Tanida, I., Mizushima, N., Kiyooka, M., Ohsumi, M., Ueno, T., Ohsumi, Y., and Kominami, E. (1999). Apg7p/Cvt2p: a novel protein-activating enzyme essential for autophagy. Mol. Biol. Cell *10*, 1367–1379.

Tanida, I., Sou, Y.S., Ezaki, J., Minematsu-Ikeguchi, N., Ueno, T., and Kominami, E. (2004). HsAtg4B/HsApg4B/autophagin-1 cleaves the carboxyl termini of three human Atg8 homologues and delipidates microtubule-associated protein light chain 3- and GABAA receptor-associated protein-phospholipid conjugates. J. Biol. Chem. *279*, 36268–36276.

Vagin, A., and Teplyakov, A. (1997). MOLREP: an automated program for molecular replacement. J. Appl. Crystallogr. *30*, 1022–1025.

von Muhlinen, N., Akutsu, M., Ravenhill, B.J., Foeglein, Á., Bloor, S., Rutherford, T.J., Freund, S.M., Komander, D., and Randow, F. (2012). LC3C, bound selectively by a noncanonical LIR motif in NDP52, is required for antibacterial autophagy. Mol. Cell *48*, 329–342.

Weiergräber, O.H., Stangler, T., Thielmann, Y., Mohrlüder, J., Wiesehan, K., and Willbold, D. (2008). Ligand binding mode of GABAA receptor-associated protein. J. Mol. Biol. *381*, 1320–1331.

Wild, P., Farhan, H., McEwan, D.G., Wagner, S., Rogov, V.V., Brady, N.R., Richter, B., Korac, J., Waidmann, O., Choudhary, C., et al. (2011). Phosphorylation of the autophagy receptor optineurin restricts Salmonella growth. Science *333*, 228–233.

Xin, Y., Yu, L., Chen, Z., Zheng, L., Fu, Q., Jiang, J., Zhang, P., Gong, R., and Zhao, S. (2001). Cloning, expression patterns, and chromosome localization of three human and two mouse homologues of GABA(A) receptor-associated protein. Genomics *74*, 408–413.